STRUCTURAL CONTROL AND HEALTH MONITORING
Struct. Control Health Monit. 2016; **00**:1–13
Published online in Wiley InterScience (www.interscience.wiley.com). DOI: 10.1002/stc

Numerical simulation of acoustic emission during crack growth in 3-point bending test

A. Berezovski[1*], M.Berezovski[2]

[1] *Laboratory of Nonlinear Dynamics, Institute of Cybernetics at Tallinn University of Technology, 21 Akadeemia Rd., Tallinn 12618, Estonia*
[2] *Department of Mathematics, Embry-Riddle Aeronautical University, 600 South Clyde Morris Blvd. Daytona Beach, FL 32114-3900, USA*

SUMMARY

Numerical simulation of acoustic emission by crack propagation in 3-point bending tests is performed to investigate how the interaction of elastic waves generates a detectable signal. It is shown that the use of a kinetic relation for the crack tip velocity combined with a simple crack growth criterion provides the formation of waveforms similar to those observed in experiments.

Received . . .

KEY WORDS: Acoustic emission, numerical simulation, wave propagation, dynamic crack

1. INTRODUCTION

Acoustic emission (AE) is widely applied in the structural health monitoring to detect individual fracture events [1, 2, 3]. One of the main sources of acoustic emission is a crack propagating in a material. Elastic waves radiated due to the moving crack tip create a signal, which can be recognized by detectors. The problem of elastic wave propagation from a moving source inside a body can be solved numerically, at least in principle. However, numerical simulations of acoustic emission do not fully capture the wave phenomena occurring during dynamic crack propagation [4]. This relates to the complexity in the dynamic crack propagation [5]. In the framework of the continuum description, a crack path and its tip velocity are the two problematic issues. While the crack path can be aligned by boundary conditions, the crack tip velocity should be determined by a kinetic relation [6].

To understand the connection between acoustic emission and crack propagation in more detail, we simulate numerically the well known 3-point bending test embedding a simple model for the crack tip velocity [7, 8]. The fracture in the 3-point bending test is in the opening mode (Mode I) of

*Correspondence to: Laboratory of Nonlinear Dynamics, Institute of Cybernetics at Tallinn University of Technology, 21 Akadeemia Rd., Tallinn 12618, Estonia. E-mail: Arkadi.Berezovski@cs.ioc.ee

loading, and the crack path can be assumed as a straight line. Such simplified description of crack propagation is used as a sample for more complicated situations. The purpose of the paper is to study the ability of the proposed model to reproduce the AE signal as the result of the interaction of elastic waves radiated by the propagating crack. Calculations are performed by means of the conservative finite-volume wave-propagation algorithm, which was proposed in [9, 10] and modified for the application to front propagation in [11, 12, 13]. The algorithm was successfully applied to wave propagation simulations in inhomogeneous solids [14]. Here the algorithm is specified for the accounting of a moving crack in two dimensions.

The paper is organised as follows. After a brief explanation of the 3-point bending test in the first Section, the governing equations of the plane strain elasticity are recalled in the second Section. The method of calculation of the dynamic J-integral is described in the third Section. Fourth Section is devoted to the kinetic relation for the straight brittle crack. The numerical procedure, initial and boundary conditions, and material parameters are presented in the fifth Section. Results of the numerical simulations are discussed in the last Section of the paper.

2. 3-POINT BENDING TEST

It should be noted that the single edge V-notched beam (SEVNB) method is the standard method for evaluating the fracture toughness [15, 16]. In the SEVNB method, the standard bend specimen is a single edge-notched and fatigue-cracked beam loaded in three-point bending with a support span, S, nominally equal to four times the width, W. The general proportions of the specimen configuration are shown in Fig. 1. The basic procedure involves loading a specimen to a selected displacement

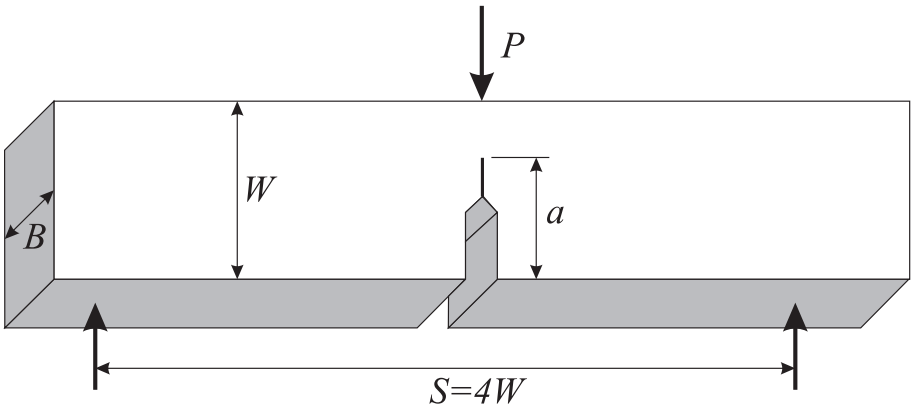

Figure 1. Specimen geometry.

level and determining the amount of crack extension that occurred during loading [17].

The stress intensity, K_I, represents the level of stress at the tip of the crack and the fracture toughness, and K_{Ic}, is the highest value of stress intensity that a material under specific (plane-strain) conditions can withstand without fracture. As the stress intensity factor reaches the K_{Ic} value, unstable fracture occurs.

For isotropic, perfectly brittle, linear elastic materials, the fracture toughness can be directly related to the J-integral if the crack extends straight ahead with respect to its original orientation.

DOI: 10.1002/stc

For plane strain under Mode I loading conditions [6]

$$J = K_I^2 \frac{1-\nu^2}{E}, \tag{1}$$

where E is the elastic modulus and ν is Poisson's ratio.

3. PLANE STRAIN ELASTICITY

Numerical simulation of the crack propagation in the 3-point bending test is based on the solution of equations of two-dimensional linear elasticity. Neglecting both geometrical and physical nonlinearities, we can write the bulk equations of homogeneous linear isotropic elasticity in the absence of body force as follows [18]:

$$\rho \frac{\partial v_i}{\partial t} = \frac{\partial \sigma_{ij}}{\partial x_j}, \tag{2}$$

$$\frac{\partial \sigma_{ij}}{\partial t} = \lambda \frac{\partial v_k}{\partial x_k} \delta_{ij} + \mu \left(\frac{\partial v_i}{\partial x_j} + \frac{\partial v_j}{\partial x_i} \right), \tag{3}$$

where t is the time, x_j are spatial coordinates, v_i are components of the velocity vector, σ_{ij} is the Cauchy stress tensor, ρ is the density, λ and μ are the Lamé coefficients.

Consider a sample that is relatively thick along x_3, and where all applied forces are uniform in the x_3 direction. Since all derivatives with respect to x_3 vanish, all fields can be viewed as functions of x_1 and x_2 only. This situation is called plane strain. The corresponding displacement component (e.g., the component u_3 in the direction of x_3) vanishes and the others (u_1, u_2) are independent of that coordinate x_3; that is,

$$u_3 = 0, \quad u_i = u_i(x_1, x_2), \quad i = 1, 2. \tag{4}$$

It follows that the strain tensor components, ε_{ij} are

$$\varepsilon_{i3} = 0, \quad \varepsilon_{ij} = \frac{1}{2}(u_{i,j} + u_{j,i}), \quad i, j = 1, 2. \tag{5}$$

The stress components follow then

$$\sigma_{3i} = 0, \quad \sigma_{33} = \frac{E}{1-2\nu} \left(\frac{\nu}{1+\nu} \varepsilon_{ii} \right), \quad i = 1, 2, \tag{6}$$

$$\sigma_{ij} = \frac{E}{1+\nu} \left(\varepsilon_{ij} + \frac{\nu}{1-2\nu} \varepsilon_{kk} \delta_{ij} \right), \quad i, j, k = 1, 2, \tag{7}$$

where E is Young's modulus, ν is Poisson's ratio, δ_{ij} is the unit tensor.

Inversion of Eq. (7) yields an expression for the strains in terms of stresses:

$$\varepsilon_{ij} = \frac{1+\nu}{E} \left(\sigma_{ij} - \nu \sigma_{kk} \delta_{ij} \right), \quad i, j, k = 1, 2. \tag{8}$$

Prepared using stcauth.cls
DOI: 10.1002/stc

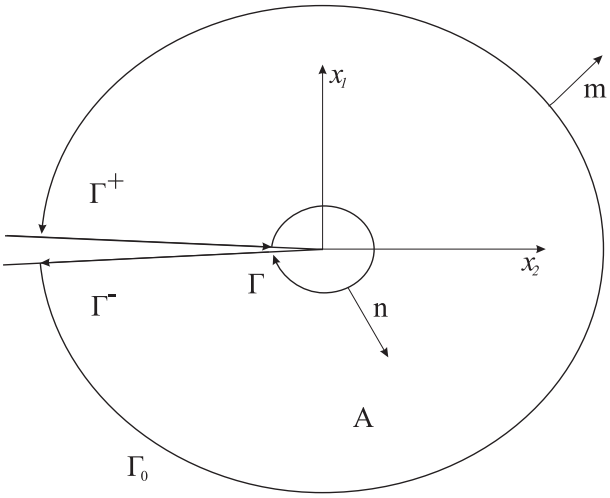

Figure 2. Crack tip coordinates and integration contours.

To simulate the crack propagation we need to apply a criterion for crack growth. We use the simple Griffith criterion [19]: When applied loading is such that

$$K_I \geq K_{Ic}, \tag{9}$$

then the crack will grow. The same criterion can be expressed in terms of the energy release rate (J-integral), because of relation (1)

$$J \geq J_c. \tag{10}$$

The J-integral is path-independent, which allows to calculate it as explained below.

3.1. Dynamic J-integral

The dynamic J-integral for a homogeneous cracked body has the physical meaning of the energy release rate [20, 21, 22]. It can be expressed in the case of Mode I straight crack as follows:

$$J = \lim_{\Gamma \to 0} \int_{\Gamma} \left((W + K)\delta_{2j} - \sigma_{ij} \frac{\partial u_i}{\partial x_2} \right) n_j d\Gamma. \tag{11}$$

Here x_2 is the coordinate in the direction of applied loading, n_j is the unit vector normal to an arbitrary contour Γ pointing outward of the enclosed domain (see Fig. 2).

The specific elastic energy stored in the body, W, and kinetic energy density, K, in a linear elastic medium are given by

$$W = \frac{1}{2}\sigma_{ij}\varepsilon_{ij}, \quad K = \frac{1}{2}\rho v_i^2. \tag{12}$$

A domain integral representation of J is more suited for numerical computation [23, 24]. Following [24], a weighting function q is introduced, which has a value of unity on the inner contour Γ and zero on the outer contour Γ_0. Within the enclosed area A, q is an arbitrary smooth function of x_1 and x_2 with values ranging from zero to one.

DOI: 10.1002/stc

Using the weighting function q, Eq. (11) can be rewritten in the form:

$$J = \lim_{\Gamma \to 0} \left(- \int_C H_{2j} m_j q \, dC + \int_{\Gamma^+ + \Gamma^-} H_{2j} m_j q \, dC \right), \tag{13}$$

where $C = \Gamma + \Gamma^+ + \Gamma^- + \Gamma_0$, vector m_j denotes the unit vector normal to C, pointing outward from the enclosed area A, and

$$H_{2j} = (W + K)\delta_{2j} - \sigma_{ij} \frac{\partial u_i}{\partial x_2}. \tag{14}$$

Components of the function H are:

$$H_{21} = (W + K)\delta_{21} - \sigma_{i1} \frac{\partial u_i}{\partial x_2} = -\sigma_{11} \frac{\partial u_1}{\partial x_2} - \sigma_{21} \frac{\partial u_2}{\partial x_2}. \tag{15}$$

$$\begin{aligned} &H_{22} = (W + K)\delta_{22} - \sigma_{i2} \frac{\partial u_i}{\partial x_2} = \\ &= (\frac{1}{2}\sigma_{1j}\varepsilon_{1j} + \frac{1}{2}\sigma_{2j}\varepsilon_{2j} + \frac{1}{2}\rho(v_1^2 + v_2^2)) - \sigma_{12} \frac{\partial u_1}{\partial x_2} - \sigma_{22} \frac{\partial u_2}{\partial x_2} = \\ &= (\frac{1}{2}\sigma_{11}\varepsilon_{11} + \frac{1}{2}\sigma_{12}\varepsilon_{12} + \frac{1}{2}\sigma_{21}\varepsilon_{21} + \frac{1}{2}\sigma_{22}\varepsilon_{22} + \frac{1}{2}\rho(v_1^2 + v_2^2)) - \sigma_{12} \frac{\partial u_1}{\partial x_2} - \sigma_{22} \frac{\partial u_2}{\partial x_2}. \end{aligned} \tag{16}$$

Applying the divergence theorem, the contour integral in Eq. (13) can be converted into an equivalent domain form [24]:

$$\begin{aligned} J &= - \int_A \left(H_{2j} \frac{\partial q}{\partial x_j} + \frac{\partial H_{2j}}{\partial x_j} q \right) dA = \\ &= - \int_A \left(H_{21} \frac{\partial q}{\partial x_1} + H_{22} \frac{\partial q}{\partial x_2} + \frac{\partial H_{21}}{\partial x_1} q + \frac{\partial H_{22}}{\partial x_2} q \right) dA. \end{aligned} \tag{17}$$

The integral over $\Gamma^+ + \Gamma^-$ vanishes because of traction-free crack surfaces.

The effect of the choice of a q function on the calculated J values is not significant [25]. In this paper, a "bell" type q function is used

$$q(x_1, x_2) = \exp(-x_1^2/b - (x_2 - a)^2/c). \tag{18}$$

where a is the position of the crack tip, b, c are parameters.

4. VELOCITY OF THE CRACK IN MODE I

To simulate crack propagation, we need to determine the crack tip velocity. In the numerical procedure, we can estimate the velocity at any time step by means of the jump relation associated with the bulk equation for linear momentum [26, 27]:

$$V_C[\rho \bar{v}_i] + N_j[\bar{\sigma}_{ij}] = 0, \tag{19}$$

DOI: 10.1002/stc

where overbars denote the values averaged over a computational cell, square brackets denote jumps, N_j is the normal to the crack front. The material velocity V_j is connected with the physical velocity v_i by [28]

$$\bar{v}_i = -(\delta_{ij} + \frac{\partial \bar{u}_i}{\partial x_j})V_j. \tag{20}$$

Inserting the latter relation into former one, we have

$$V_C \left[\rho(\delta_{ij} + \frac{\partial \bar{u}_i}{\partial x_j})V_j\right] - N_j[\bar{\sigma}_{ij}] = 0. \tag{21}$$

In the case of a straight crack in Mode I the last expression reduces to

$$V_C^2 = \frac{\bar{\sigma}_{22}}{\rho(1+\bar{\varepsilon}_{22})}, \tag{22}$$

where V_C is the crack tip velocity and σ_{22} and ε_{22} are stress and strain components in the direction of the crack propagation, respectively.

These stress and strain components at the crack tip are not determined due to the square-root singularity. As it is shown [7], if we apply a local equilibrium approximation for σ_{22} and linear stress-strain relation for ε_{22}, we will arrive at the kinetic relation

$$\frac{V_C^2}{c_R^2} = \frac{\bar{\sigma}_{22}}{\bar{\sigma}_{22} + \rho_0 c_R^2}, \tag{23}$$

with the Rayleigh velocity c_R as the limiting crack tip velocity. Here $\bar{\sigma}_{22}$ is the local equilibrium (averaged) value of the stress component.

As experiments show [29], the limiting velocity of the crack tip is usually significantly less than the Rayleigh speed. This leads to a generalization of the kinetic relation (23) by introducing a limiting crack speed V_T

$$\frac{V_C^2}{V_T^2} = \frac{\sigma_{22}}{\sigma_{22} + \rho_0 V_T^2}, \tag{24}$$

but the stress component σ_{22} at the crack tip is no more an equilibrium one. To determine its value, we apply an assumption analogous to that in the case of the phase boundary [8]

$$\sigma_{22} = N f_C, \tag{25}$$

where f_C is the driving force acting at the crack tip and N is a material dependent coefficient.

In the thin strip geometry, the driving force is related to the J-integral (e.g. [30])

$$f_C = \frac{J}{l}, \tag{26}$$

where l is a scaling factor with dimension of length.

Accordingly, we arrive at the kinetic relation

$$\frac{V_C^2}{V_T^2} = \frac{NJ/l}{NJ/l + \rho_0 V_T^2} = 1 - \left(\frac{1}{1 + NJ/\rho_0 V_T^2 l}\right). \tag{27}$$

DOI: 10.1002/stc

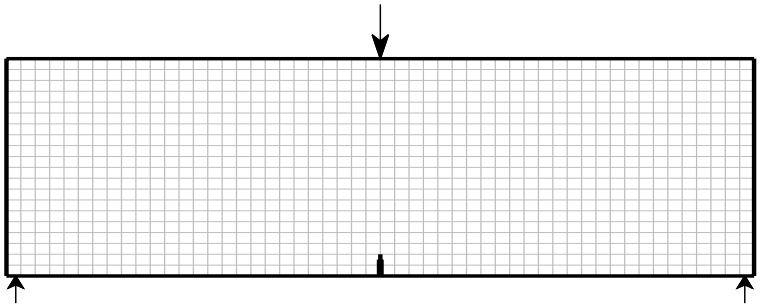

Figure 3. Sketch of computational domain.

The characteristic length l can be related to the process zone length [31]

$$l \sim \frac{K_{Ic}^2}{\sigma_f^2}, \tag{28}$$

with the critical value of the stress intensity factor K_{Ic} and the applied stress σ_f.

The value of the applied stress σ_f, in its turn, can be expressed in terms of the dynamic release rate (1). Correspondingly, the kinetic relation (27) can be rewritten as (cf. [7])

$$\frac{V_C^2}{V_T^2} = 1 - \left(1 + M\frac{J^2}{J_c}\right)^{-1}, \tag{29}$$

where the coefficient M depends on the properties of material.

5. NUMERICAL SIMULATION OF CRACK PROPAGATION

To compute the value of the J-integral by means of Eqs. (14)-(18), we need to know the strain and stress fields. For this purpose, system of Eqs. (2)-(3), specialized to plane strain conditions by Eqs. (4)-(8), is solved numerically by means of the conservative finite-volume wave-propagation algorithm. The advantages of the wave-propagation algorithm are its stability up to the Courant number equal to unity, high-order accuracy, and energy conservation [10]. It should be noted that discrete element method, which is the basis of lattice model simulations (see [32], e.g.), provides equivalent results for continuum dynamic problems, as shown in [33].

The corresponding two-dimensional computational domain is shown in Fig. 3. Loading is applied at the middle of the upper boundary. Initial crack is placed at the middle of the bottom. Boundaries are stress free except the left and right ends of the bottom boundary, which are fixed. Initially, the beam is at rest yielding zero initial values of wanted fields on all cells. The solution includes two steps. First, numerical fluxes at boundaries between cells are computed. Then new averaged stresses, strains and velocities on all cells are evaluated. Their values at the boundaries are computed using boundary conditions. The solution procedure is described in detail in [14].

The size of the beam is chosen as follows: length S = 250 mm, height W = 60 mm, width B = 30 mm. Silica aerogel is chosen as the material of the beam. Its properties are extracted from [34]:

Prepared using stcauth.cls
DOI: 10.1002/stc

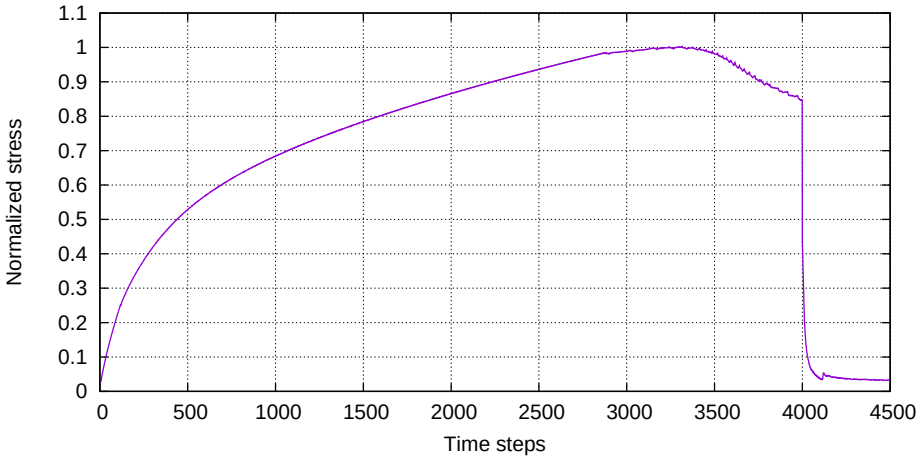

Figure 4. Load time history.

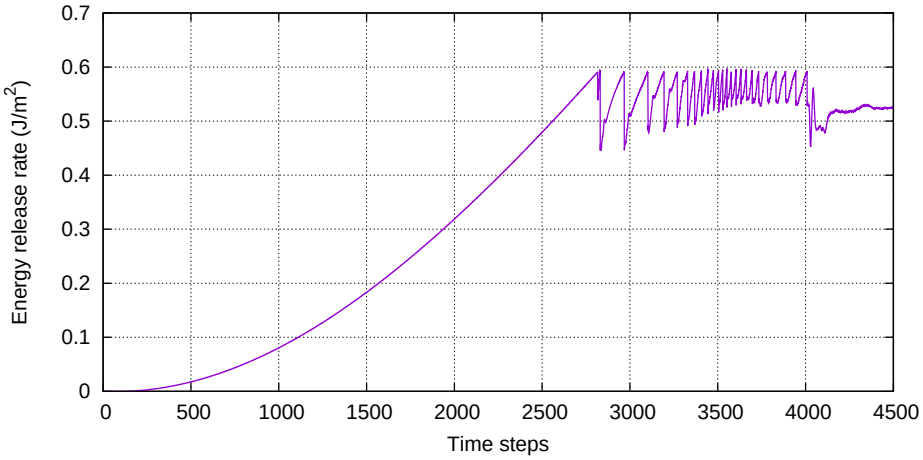

Figure 5. Time history of the energy release rate.

the density ρ is 200 kg/m^3), Young's Modulus E is 6.5 MPa, Poisson's ratio is 0.2, the fracture toughness K_c is 2 KPa-m$^{1/2}$.

For numerical simulation, the space step Δx is chosen as 1 mm and the corresponding time step is determined from the value of the Courant number equal to 1. This gives the value of the time step as $\Delta t = \Delta x/c_p$. In the case of silica aerogel c_p = 180 m/s, which results in the value of the time step $\Delta t = 0.5\,10^{-5}$ s. The loading is determined by the cross-head velocity, which constant value is chosen as 0.294 m/s. The time history of the loading in terms of the normalized stress in the middle of the upper boundary is presented in Fig. 4. The loading is eliminated at 4000 time steps to avoid the complete breaking down of the specimen.

The value of the J-integral is computed by means of Eqs. (14)-(18) at every time step. If this value overcomes its critical value, then the crack starts to propagate. The velocity of the crack propagation is calculated by means of Eq. (29) with the value of dimensionless coefficient $M = 0.375$. A simple procedure for the tracking of the crack tip is applied. Its virtual displacement is computed for each time step. We keep the location of the crack tip in the old place if the sum of its virtual

DOI: 10.1002/stc

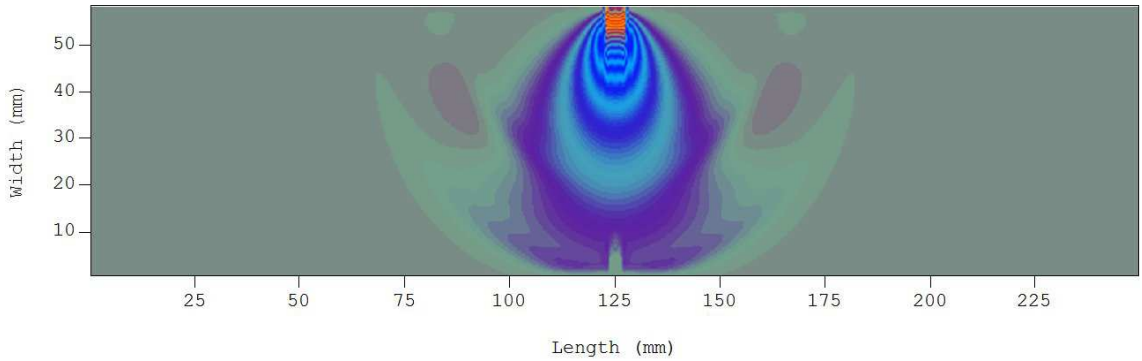

Figure 6. Stress field at 60 time steps.

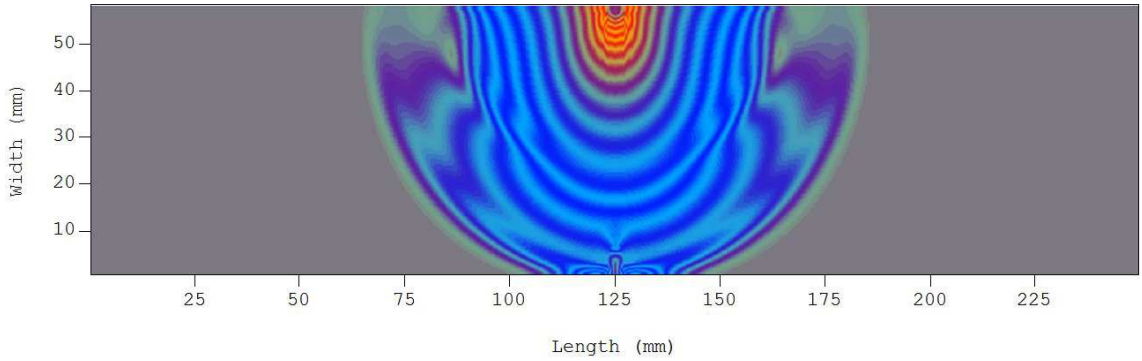

Figure 7. Wave field at 60 time steps.

displacements is less than the size of space step, and change it to one space step forward otherwise. All the calculations are performed with the Courant number equal to 1.

6. RESULTS AND DISCUSSION

Time history of the J-integral presented in Fig. 5 shows that initially its value is increased with time like a square of time. The crack starts to grow if the critical value of the J-integral is reached. The crack growth is accompanied by a sudden decrease of the value of the J-integral due to the stress relaxation. It means that the crack is not growing until the value of the J-integral could reach its critical value again. The process is repeating until 4000 time steps; after that the loading is eliminated. The similar discontinuous behavior of the crack in the 3-point bending test is mentioned in [35].

Typical wave propagation from a point source in the middle of the upper boundary is observed for first 500 time steps. As an example, normal stress distribution and wave field (in fact, the energy distribution) for 60 steps are given in Figs. 6 and 7. Then a stabilized wave field is formed and kept for next 2300 time steps. The corresponding normal stress distribution and wave field for 1600 time steps are shown in Figs. 8 and 9.

DOI: 10.1002/stc

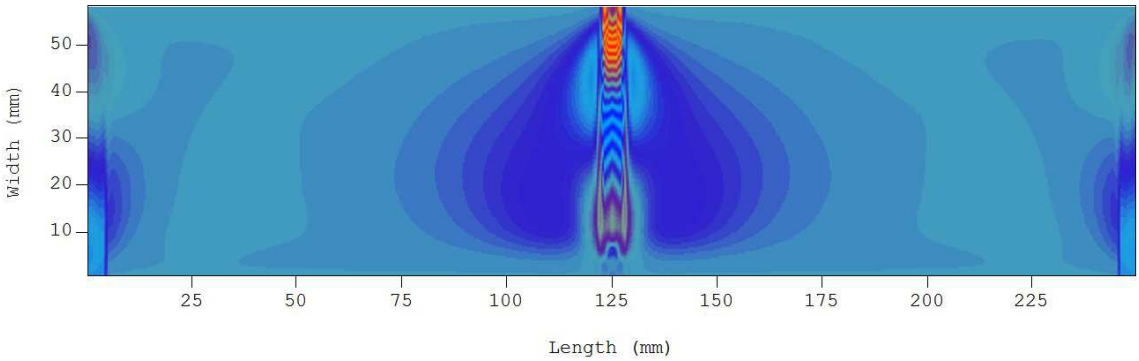

Figure 8. Stress field at 1600 time steps.

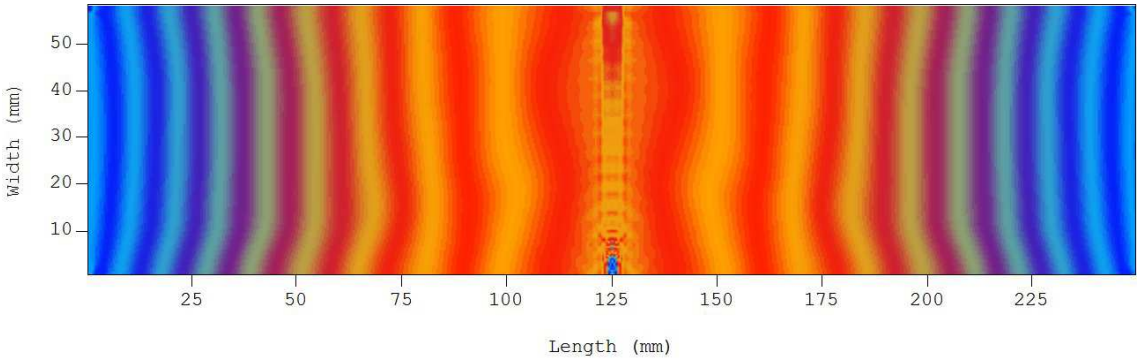

Figure 9. Wave field at 1600 time steps.

The crack starts to grow approximately at 2815 time steps that is reflected in the radiation of short waves from the crack tip. The interaction of these radiated waves with the global wave field established before is displayed in supplementary animated picture, which shows the evolution of wave field from 2800 till 4000 time steps as well as the crack propagation. The growing size of the crack is also clearly seen. Typical example of normal stress distribution at 4000 time steps is given in Fig. 10.

Waves emitted by the growing crack due to their interference and reflection from boundaries form the wave pattern shown in Fig. 11. In the middle of the side boundaries they generate a signal presented in Fig. 12 in terms of the normal stress. This waveform looks qualitatively similar to those registered in experiments [36]. This means that numerical simulation of the crack propagation under the 3-point bending test conditions can predict acoustic emission even in the framework of a simple macroscopic model for the crack tip velocity. Despite the simplified representation of the fracturing process, it provides the possibility to calculate the signal as a result of interaction of elastic waves. The 3-point bending test is chosen for the numerical simulation because it is the standard procedure for the determination of the fracture toughness of materials.

It should be noted that the dissipation of energy due to the crack propagation is controlled by the velocity of the crack tip and the driving force (the energy release rate). The applied numerical procedure of the crack tip tracking provides only an estimate of the dissipated energy. A more accurate discontinuity tracking procedure with the mesh adaptation is needed for more detailed results. Such a procedure, which is crucial for a non-straight crack path, is under development.

DOI: 10.1002/stc

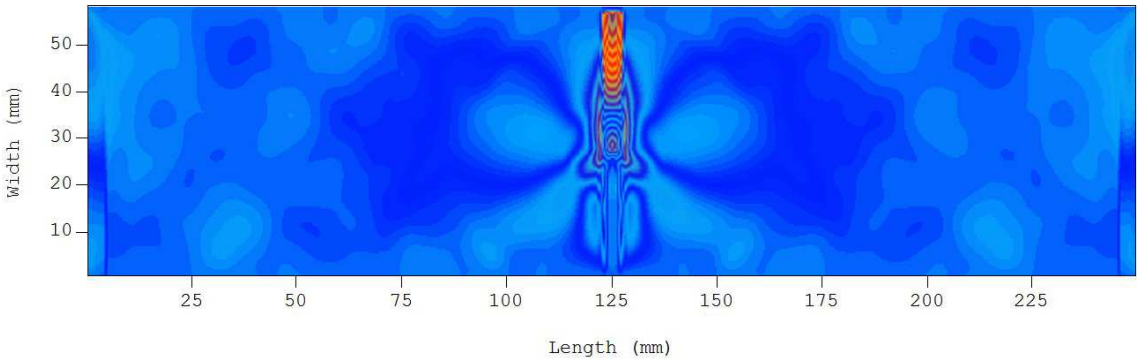

Figure 10. Stress field at 4000 time steps.

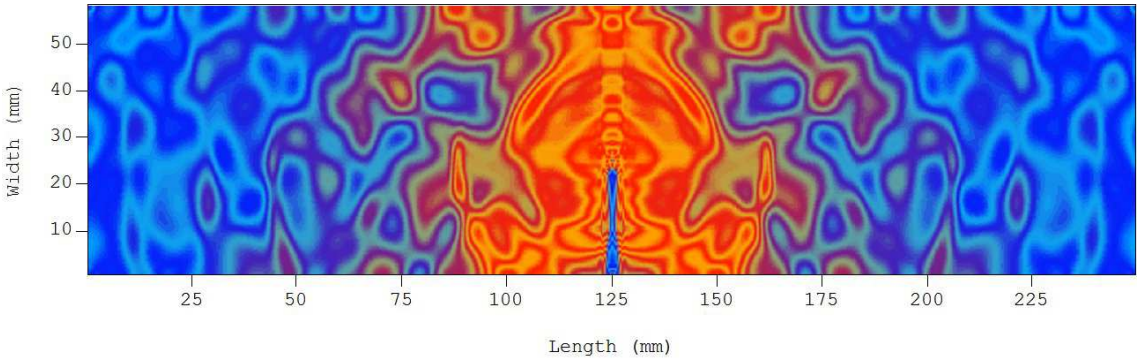

Figure 11. Wave field at 4000 time steps.

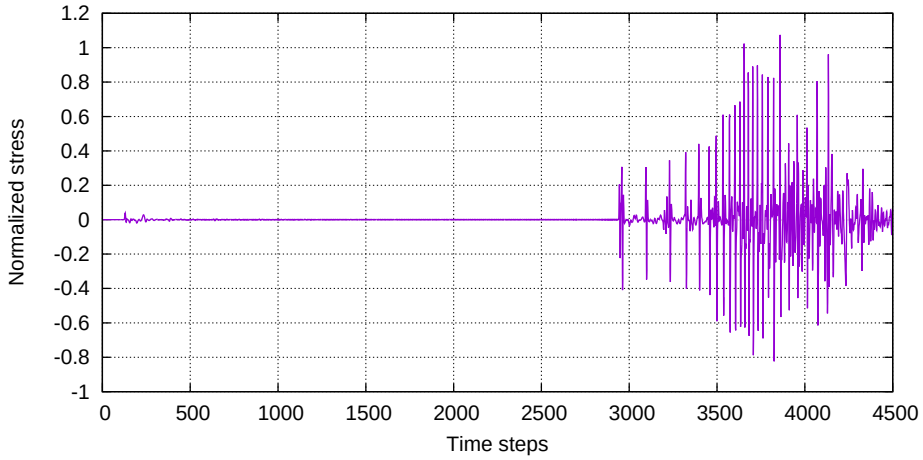

Figure 12. Time history of the normal stress at the boundary.

ACKNOWLEDGMENTS

The research was supported by the EU through the European Regional Development Fund and by the Estonian Research Council (grant PUT434).

REFERENCES

Prepared using stcauth.cls
DOI: 10.1002/stc

1. Grosse, C.U. and Ohtsu, M. (2008) *Acoustic Emission Testing*, Springer Science & Business Media.
2. Ono, K. (2011) Acoustic emission in materials research–a review. *Journal of Acoustic Emission*, **29**, 284–308.
3. Ono, K. and Gallego, A. (2012) Research and applications of ae on advanced composites. *Journal of Acoustic Emission*, **30**, 180–230.
4. Lisjak, A., Liu, Q., Zhao, Q., Mahabadi, O., and Grasselli, G. (2013) Numerical simulation of acoustic emission in brittle rocks by two-dimensional finite-discrete element analysis. *Geophysical Journal International*, **195** (1), 423–443.
5. Fineberg, J. and Bouchbinder, E. (2015) Recent developments in dynamic fracture: some perspectives. *International Journal of Fracture*, **196** (1-2), 33–57.
6. Freund, L.B. (1998) *Dynamic Fracture Mechanics*, Cambridge University Press.
7. Berezovski, A. and Maugin, G.A. (2007) On the propagation velocity of a straight brittle crack. *International Journal of Fracture*, **143** (2), 135–142.
8. Berezovski, A. and Maugin, G.A. (2010) Jump conditions and kinetic relations at moving discontinuities. *ZAMM-Journal of Applied Mathematics and Mechanics/Zeitschrift für Angewandte Mathematik und Mechanik*, **90** (7-8), 537–543.
9. LeVeque, R.J. (1997) Wave propagation algorithms for multidimensional hyperbolic systems. *Journal of Computational Physics*, **131** (2), 327–353.
10. LeVeque, R.J. (2002) *Finite Volume Methods for Hyperbolic Problems*, Cambridge University Press.
11. Berezovski, A., Engelbrecht, J., and Maugin, G. (2000) Thermoelastic wave propagation in inhomogeneous media. *Archive of Applied Mechanics*, **70** (10), 694–706.
12. Berezovski, A. and Maugin, G. (2001) Simulation of thermoelastic wave propagation by means of a composite wave-propagation algorithm. *Journal of Computational Physics*, **168** (1), 249–264.
13. Berezovski, A. and Maugin, G.A. (2002) Thermoelastic wave and front propagation. *Journal of Thermal Stresses*, **25** (8), 719–743.
14. Berezovski, A., Engelbrecht, J., and Maugin, G.A. (2008) *Numerical Simulation of Waves and Fronts in Inhomogeneous Solids*, World Scientific.
15. Morrell, R. (2006) Fracture toughness testing for advanced technical ceramics: internationally agreed good practice. *Advances in Applied Ceramics*, **105** (2), 88–98.
16. Xu, J., Tang, D., Lee, K.J., Lim, H.B., Park, K., and Cho, W.S. (2012) Comparison of fracture toughness evaluating methods in 3Y-TZP ceramics reinforced with Al_2O_3 particles. *Journal of Ceramic Processing Research*, **13** (6), 683–687.
17. ASTM Standard E1820, 2011e1 (2011) "Standard test method for measurement of fracture toughness", in *ASTM International*, West Conshohocken, PA.
18. Barber, J.R. (2009) *Elasticity*, Springer.
19. Zehnder, A.T. (2012) *Fracture Mechanics*, Springer.
20. Atkinson, C. and Eshelby, J. (1968) The flow of energy into the tip of a moving crack. *International Journal of Fracture Mechanics*, **4** (1), 3–8.
21. Freund, L. (1972) Energy flux into the tip of an extending crack in an elastic solid. *Journal of Elasticity*, **2** (4), 341–349.
22. Maugin, G. (1994) On the j-integral and energy-release rates in dynamical fracture. *Acta Mechanica*, **105** (1-4), 33–47.
23. Nakamura, T., Shih, C.F., and Freund, L. (1985) Computational methods based on an energy integral in dynamic fracture. *International Journal of Fracture*, **27** (3-4), 229–243.
24. Moran, B. and Shih, C. (1987) A general treatment of crack tip contour integrals. *International Journal of Fracture*, **35** (4), 295–310.
25. Shih, C., Moran, B., and Nakamura, T. (1986) Energy release rate along a three-dimensional crack front in a thermally stressed body. *International Journal of Fracture*, **30** (2), 79–102.
26. Maugin, G. (1997) Thermomechanics of inhomogeneous-heterogeneous systems: application to the irreversible progress of two-and three-dimensional defects. *ARI-An International Journal for Physical and Engineering Sciences*, **50**, 41–56.
27. Maugin, G. (1998) On shock waves and phase-transition fronts in continua. *ARI-An International Journal for Physical and Engineering Sciences*, **50** (3), 141–150.
28. Maugin, G.A. (1993) *Material Inhomogeneities in Elasticity*, CRC Press.
29. Ravi-Chandar, K. (2004) *Dynamic Fracture*, Elsevier.
30. Maugin, G. (2000) On the universality of the thermomechanics of forces driving singular sets. *Archive of Applied Mechanics*, **70** (1-3), 31–45.

31. Awaji, H., Nishimura, Y., Choi, S.M., Takahashi, Y., Goto, T., and Hashimoto, S. (2009) Toughening mechanism and frontal process zone size of ceramics. *Journal of the Ceramic Society of Japan*, **117** (1365), 623–629.
32. Birck, G., Iturrioz, I., Lacidogna, G., and Carpinteri, A. (2016) Damage process in heterogeneous materials analyzed by a lattice model simulation. *Engineering Failure Analysis*, **70**, 157–176.
33. Liu, K. and Liu, W. (2006) Application of discrete element method for continuum dynamic problems. *Archive of Applied Mechanics*, **76** (3), 229–243.
34. Phalippou, J., Woignier, T., and Rogier, R. (1989) Fracture toughness of silica aerogels. *Le Journal de Physique Colloques*, **50** (C4), 191–196.
35. Carpinteri, A., Lacidogna, G., Corrado, M., and Di Battista, E. (2016) Cracking and crackling in concrete-like materials: A dynamic energy balance. *Engineering Fracture Mechanics*, **155**, 130–144.
36. Kishi, T., Ohtsu, M., and Yuyama, S. (2000) *Acoustic Emission-Beyond the Millennium*, Elsevier.

DOI: 10.1002/stc